Thermal stability of Na3-xV2(PO4)2F3-yOy: influence of F- for O2- substitution and degradation mechanisms

Chloé Pablos, Jacob Olchowka, Emmanuel Petit, Gaël Minart, Mathieu Duttine, François Weill, Christian Masquelier, Dany Carlier, Laurence Croguennec

Thermal stability of $Na_{3-x}V_2(PO_4)_2F_{3-y}O_y$: influence of F^- for O^{2-} substitution and degradation mechanisms

Chloé Pablos [a,b,c], Jacob Olchowka [a,c,d*], Emmanuel Petit [a,c], Gaël Minart [a,c], Mathieu Duttine [a], François Weill [a,c], Christian Masquelier [b,c,d], Dany Carlier [a,c,d], Laurence Croguennec [a,c,d*]

[a] Univ. Bordeaux, CNRS, Bordeaux INP, ICMCB, UMR 5026, F-33600 Pessac, France

[b] Laboratoire de Réactivité et de Chimie des Solides, Université de Picardie Jules Verne, CNRS-UMR 7314, F-80039 Amiens Cedex 1, France

[c] RS2E, Réseau Français sur le Stockage Electrochimique de l'Energie, CNRS FR 3459, 80039 Amiens Cedex 1, France

[d] ALISTORE-ERI European Research Institute, CNRS FR 3104, 80039 Amiens Cedex 1, France

KEYWORDS: *sodium-ion battery, positive electrode material, vanadium phosphates, thermal stability, degradation mechanism, $Na_3V_2(PO_4)_2F_3$*

ABSTRACT: The Na-ion battery technology appears as a reliable, sustainable and environmentally friendly alternative to the Li-ion one, especially for stationary energy storage. As for the Li-ion technology, safety aspect is of high importance to ensure large-scale development. In this work, we studied the thermal stability and decomposition mechanisms of carbon-coated $Na_3V_2(PO_4)_2F_3$ and two fluorine-rich phases belonging to the solid-solution $Na_3V^{3+}_{2-y}V^{4+}_y(PO_4)_2F_{3-y}O_y$ (y = 0.07 and y = 0.12), that family of compounds being often considered among the most promising positive electrode materials for Na-ion batteries. This study shows the good thermal stability of these polyanionic materials and reveals that a low O^{2-} for F^- substitution has a very limited effect on the thermal stability of fully re-intercalated materials recovered in the discharged state of the battery, whereas it has a beneficial impact for highly de-intercalated ones, obtained by in-depth charges. Furthermore, whatever the state of charge and the oxygen content in $Na_xV_2(PO_4)_2F_{3-y}O_y$ ($1 \leq x \leq 3$ and y = 0, 0.07 and 0.12), the thermal degradation leads, quite unexpectedly, to the formation of crystalline $Na_3V^{3+}_2(PO_4)_2F_3$ in addition to an amorphous phase. The fluorination of the partially oxygen for fluorine substituted material was clearly demonstrated by X-ray diffraction (XRD) and solid state nuclear magnetic resonance spectroscopy (NMR) on materials recovered after differential scanning calorimetry (DSC) analyses. The formation of a fully sodiated crystalline phase from the thermal degradation of the material obtained in charged states of the battery, with or without presence of electrolyte, was never reported before.

Corresponding Authors

* laurence.croguennec@icmcb.cnrs.fr
* Jacob.olchowka@icmcb.cnrs.fr

INTRODUCTION

$Na_3V_2(PO_4)_2F_3$ (NVPF) is currently considered as one of the more efficient positive electrode material for practical use in Na-ion batteries.[1–3] Its attractive theoretical capacity of 128 mAh/g, obtained by the reversible extraction of two Na^+ ions per formula unit at an average potential of 3.95 V *vs* Na^+/Na, leads to a theoretical energy density of ~500 Wh/kg, which is comparable to that delivered by $LiFePO_4$ in Li-ion batteries. Since the first report of $Na_3V_2(PO_4)_2F_3$ as a positive electrode material in full cells vs hard carbon in 2013,[4] a lot of work has been done to characterize the crystal structure of NVPF, to understand the reaction mechanisms involved upon electrochemical operation and to optimize its energy storage performance. [5–14] All these achievements led to the development of the first 18650 prototypes made of carbon-coated NVPF vs. hard carbon, that exhibit very promising power performances which led to the creation of the French start-up company Tiamat.[15] Although a lot of research is still done to optimize NVPF rate capability by tailoring particle morphologies or conductive coatings,[16–22] few has been reported on NVPF thermal stability upon electrochemical operation, which is crucial for practical applications.[23–27] Traditionally, polyanionic electrode materials are considered as safer than layered oxides due a strong covalent bonding of oxygen to phosphorus in the PO_4 group that limits the generation of flammable gases (oxygen release) during thermal degradation.[26,28,29] Nevertheless, the degradation mechanisms of NVPF need to be investigated at different states of charge or discharge of the battery, to determine the reactions involved during a thermal runaway and confirm or not the good thermal and structural stability of the sodium vanadium fluoride phosphate materials.

The crystal structure of NVPF is built with $V_2O_8F_3$ bi-octahedral units connected by PO_4 groups that lead to the formation of a stable three-dimensional framework with large channels allowing fast sodium ions diffusion (mostly 2-D) and an excellent stability upon long-term cycling.[5] Additionally, NVPF can easily accommodate various chemical substitutions such as O^{2-} for F^- that allows the preparation of the solid-solution $Na_3V^{3+}_{2-y}V^{4+}_y(PO_4)_2F_{3-y}O_y$ ($0 \leq y \leq 2$).[30–36] Depending on the synthesis conditions, this substitution can be either finely tuned or not, leading to discrepancies in lattice parameters and electrochemical signatures reported in the literature.[6,16,37]

It was previously demonstrated that O^{2-} for F^- substitution in $Na_3V^{3+}_{2-y}V^{4+}_y(PO_4)_2F_{3-y}O_y$ does not significantly impact the specific capacity since two Na^+ ions can be reversibly extracted whatever the oxygen content.[33,38] On the other hand, a partial O^{2-} for F^- substitution allows to improve the structural stability at high potential and enhances the electrical conductivity.[33,39] However, the higher the oxygen content, the lower is the average working potential.[39] Thus, to avoid energy density penalties, $Na_3V_2(PO_4)_2F_3$ and F-rich phases (with a low O^{2-} for F^- substitution) are the most suitable for practical purposes.

In this work, we investigated the thermal stability of carbon-coated $Na_3V_2(PO_4)_2F_3$ and two carbon-coated fluorine-rich phases belonging to the solid-solution $Na_3V^{3+}_{2-y}V^{4+}_y(PO_4)_2F_{3-y}O_y$ (y = 0.07 and y = 0.12). The impact of a low oxygen for fluorine substitution on the thermal stability was investigated by differential scanning calorimetry (DSC), for electrode materials recovered at various states of charge and in contact with the electrolyte. *In situ* X-ray diffraction (XRD) and a large panel of *post mortem* analyses were also used to thoroughly characterize and understand the unusual degradation mechanisms occurring upon heating.

EXPERIMENTAL

Material synthesis. Carbon-coated $Na_3V_2(PO_4)_2F_{3-y}O_y$ ($NVPFO_y/C$) materials were prepared by a one-step solid-state reaction according to the following reaction, determined by Nguyen et *al.*[39] :

$$\left(2-\frac{y}{2}\right)VPO_4/C+\frac{y}{2}VOPO_4+\left(3-\frac{y}{2}\right)NaF+\frac{y}{4}Na_2CO_3+\frac{y}{4}H_2O_{media}\rightarrow Na_3V^{3+}{}_{2-y}V^{4+}{}_y(PO_4)_2F_{3-y}O_y+\frac{y}{4}CO_2+\frac{y}{2}HF$$

The oxygen content ("y" in the chemical formula $Na_3V_2(PO_4)_2F_{3-y}O_y$) was controlled by tailoring the molar ratio between the precursors. $VOPO_4$, bare VPO_4 and VPO_4/C were obtained from homemade $VOPO_4{\cdot}2H_2O$, this latter being synthesized by heating V_2O_5 under reflux with phosphoric acid and distilled water at 100°C for 3 hours according to ref [40]. $VOPO_4{\cdot}2H_2O$ was dehydrated by a thermal treatment at 250°C for 2 hours to obtain $VOPO_4$, which was then reduced under Ar/5%H_2 flow at 890°C for 2 hours to get VPO_4. Sucrose (10 wt.%) was added during this last step to obtain VPO_4/C. The final carbon content was determined (by Thermogravimetry) for NVPF/C to be 2.6 wt.%.

To obtain NVPF-type powders, stoichiometric amounts of $VOPO_4$, carbon-coated VPO_4 (c-VPO_4), NaF (Sigma Aldrich; ≥ 99%) and Na_2CO_3 (Sigma Aldrich; ≥ 99%) were grinded mechanically (SPEX) for 90 minutes within an agate jar. Then, the mixture was pelletized, placed in a gold crucible and heated at 600°C for 3 hours under Argon flow.

Powder X-ray diffraction (PXRD) patterns were recorded using either a PANalytical X'Pert PRO MPD diffractometer in Bragg-Brentano θ-θ geometry (acquisition being performed in the 2θ range of 10-80° with a step size of 0.0167°) or a PANalytical XPert 3 diffractometer in Debye-Scherrer θ-θ geometry (acquisition being performed on powder packed in a 0.3 mm diameter capillary in the 2θ range of 10-60° with a step size of 0.0167°). Both diffractometers were equipped with a Cu-$K_{\alpha1,2}$ X-ray source. Le Bail refinements were performed using Jana2006[14].

In situ temperature XRD was performed by adding an Anton-Paar heating chamber on the PANalytical XPert 3 diffractometer in Debye-Scherrer θ-θ geometry. Patterns were recorded during 1h30, in the 2θ range of 10-80° with a step size of 0.0167°, after a 10°C/min temperature increase or decrease followed by a 10min stabilization step at the chosen temperature (the acquisition temperatures have been chosen according to the DSC measurements).

Scanning electron microscopy (SEM) images were obtained with a Tescan Vega instrument after a gold deposition on the surface of the polycrystalline samples.

Transmission electron microscopy (TEM) images were obtained with a JEOL 2100 microscope. Before the observation, the material was dispersed in ethanol and a drop was deposited on a copper grid with a carbon supported film.

Solid-state nuclear magnetic resonance spectroscopy (NMR). ^{31}P MAS NMR spectra were recorded on a Bruker Avance III spectrometer equipped with a 2.4 T wide-bore magnet (Larmor frequency of 40.6 MHz for ^{31}P). Experiments were performed using a 2.5 mm magic-angle spinning (MAS) probe, and zirconia rotors with a 30 kHz spinning frequency. A one-period of rotation synchronized Hahn echo sequence was used with a 2 µs 90° pulse and a recycle delay of 0.5 s long enough to ensure to avoid T_1

saturation effects. H_3PO_4 85% (Sigma-Aldrich) was used as reference for 0 ppm chemical shift. ^{23}Na MAS NMR spectra were recorded on a Bruker Avance III spectrometer equipped with a 11.7 T wide-bore magnet (Larmor frequency of 132.3 MHz for ^{23}Na). Experiments were performed using a 2.5 mm MAS probe, with a 30 kHz spinning frequency. A short pulse length of 1.1 μs corresponding to a selective $\pi/8$ pulse determined by using a 0.1 M NaCl aqueous solution was employed. The spectral width was set to 1 MHz and the recycle delay of 0.5 s, which was long enough to avoid T_1 saturation effects. The baseline distortions resulted from the spectrometer dead time (5-10 μs) were removed computationally by using a polynomial baseline correction routine. An aqueous 0.1M NaCl solution was used as reference for 0 ppm chemical shift.

Raman spectroscopy data were obtained with a confocal LabRAM HR Evolution micro-spectrometer from Horiba, using a 633 nm laser source. They were collected in the range 150-2000 cm^{-1}, using a 10.6 mm (NA 0.5) focal length lens and with an acquisition time of 20 s and 30 accumulations. Raman spectroscopy analyses were performed on pellets for pristine materials and materials recovered after DSC treatments, whereas they were performed on powders packed in 0.5 mm diameter capillaries sealed in a glove box under Ar atmosphere for materials recovered after cycling.

Battery preparation. Electrodes were prepared using the tape casting method. 80 wt.% of active material ($NVPFO_y$/C), 10 wt.% of carbon black and 10 wt.% of polyvinylidene fluorine (Sigma Aldrich; Mw = 534 000 $g.mol^{-1}$) were mixed in N-methyl-2-pyrrolidone (Sigma Aldrich; 99% anhydrous) for 2 hours. The slurry was casted on an aluminum foil and dried at 80°C overnight. The loading of the electrodes was around 5-6 $mg.cm^{-2}$ and the porosity around 30-35%. The cells were assembled in an argon filled glovebox in CR2032-type coin cells with sodium metal used as negative electrode and 150 µL of electrolyte. The electrolyte is made of 1M $NaPF_6$ in ethylene carbonate and dimethyl carbonate (EC:DMC) with 2 wt.% of fluoroethylene carbonate (FEC) as additive. The assembled cells were cycled in galvanostatic mode at C/20, between 2.5 and 4.3 V, with potentiostatic steps at the cut-off potential until an almost zero charge current is reached.

Differential scanning calorimetry (DSC) was carried out using a DSC Pyris Diamond calorimeter within 50-350°C temperature range with a heating rate of 10°C.min^{-1} under an argon flow (40 mL.min^{-1}). Samples were prepared in an argon filled glovebox by placing approximatively 8-12 mg of powder removed from the current collector, without any drying or washing, into two sealed high-pressure stainless-steel crucibles, to check for the reproducibility of the results.

RESULTS AND DISCUSSIONS

The PXRD patterns of the carbon-coated $Na_3V^{3+}_{2-y}V^{4+}_y(PO_4)_2F_{3-y}O_y$ ($NVPFO_y$/C, y = 0, 0.07 and 0.12) compounds are displayed in **figure 1a** and confirm the successful synthesis of expected phases. They can all be indexed in the *Amam* space group,[6] in good agreement with the previously discovered orthorhombic distortion of the unit cell.[39] The results of the full pattern matching (Le Bail) refinements are compared in **figure S1** and the cell parameters are listed in **Table 1**.

As reported previously, the oxygen content within the solid solution $Na_3V^{3+}_{2-y}V^{4+}_y(PO_4)_2F_{3-y}O_y$ and thus the chemical composition can be determined from the values of the lattice parameters, due to a linear

evolution of both the c-lattice parameter and the unit cell volume as function of the oxygen content (**figures 1b-c**).[9,31,33,39] Based on the result of the full pattern matching refinements, $Na_3V^{3+}_2(PO_4)_2F_3$/C (NVPF/C), $Na_3V^{3+}_{1.93}V^{4+}_{0.07}(PO_4)_2F_{2.93}O_{0.07}$/C ($NVPFO_{0.07}$/C) and $Na_3V^{3+}_{1.88}V^{4+}_{0.12}(PO_4)_2F_{2.88}O_{0.12}$/C ($NVPFO_{0.12}$/C) were successfully synthetized, which is in rather good agreement with the targeted compositions (**Table 1**). SEM images of the three compounds are given in **figure S2** and reveal that particles' size tends to slightly decrease by increasing the oxygen content.

Table 1 (to be included in the published version as a two-column table): Lattice parameters and chemical formula of the three studied compositions $Na_3V^{3+}_{2-y}V^{4+}_y(PO_4)_2F_{3-y}O_y$ determined by Le Bail refinement of their PXRD patterns and comparison of the cell parameters (c and V/Z values), respectively.

Sample	y target	Space group	a (Å)	b (Å)	c (Å)	V/Z (Å³)	y value	Composition
NVPF/C	0	*Amam*	9.0279(8)	9.0411(6)	10.7520(8)	219.5(2)	0	$Na_3V_2(PO_4)F_3$
$NVPFO_{0.07}$/C	0.05	*Amam*	9.0301(8)	9.0461(8)	10.7454(6)	219.5(1)	0.07	$Na_3V_2(PO_4)F_{2.93}O_{0.07}$
$NVPFO_{0.12}$/C	0.1	*Amam*	9.0303(8)	9.0462(8)	10.7419(6)	219.4(1)	0.12	$Na_3V_2(PO_4)F_{2.88}O_{0.12}$

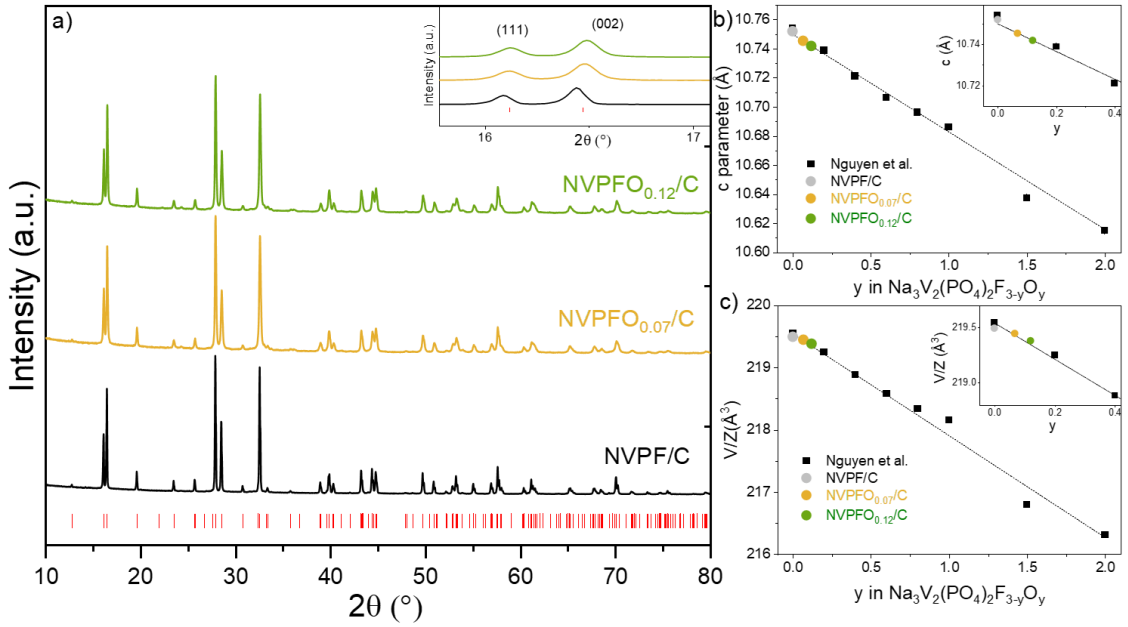

Figure 1: a) X-ray diffraction patterns of NVPF/C (black), $NVPFO_{0.07}$/C (yellow) and $NVPFO_{0.12}$/C (green). The inset shows the *(111)* and *(002)* reflections. b-c) Comparison, with those reported by Nguyen *et al.*[39], of the c-lattice parameter and cell volume per formula unit (V/Z) determined for each compound by a full pattern matching (Le Bail) refinement.

The ^{31}P NMR spectra recorded for the three pristine compounds (**Figure 2a**) support the compositions determined by X-ray diffraction. The spectrum of NVPF/C displays one main signal at 6000 ppm whereas partially F/O substituted materials exhibit two other isotropic signals at 4500 and 3000 ppm, which are the result of different interactions at the atomic local environment between paramagnetic V^{3+} (in red) and V^{4+} (in blue) ions with ^{31}P nuclei (in green).[41] These signals are respectively attributed to phosphorous environments surrounded by four V^{3+} ions (6000 ppm), by one V^{4+} and three V^{3+} ions (4500 ppm), and two V^{4+} and two V^{3+} ions (3000 ppm),[41,42] confirming the mixed valence state of the

vanadium and thus, a partial oxygen for fluorine substitution. This signals' assignment has been previously confirmed by DFT calculations that also revealed that V^{4+} ions have a specific electronic structure as involved in vanadyl bonds.[39] Note that NVPF/C spectrum presents also a very low intensity signal around 4500 ppm, indicating traces of oxygen defaults in the material as already reported. [40]

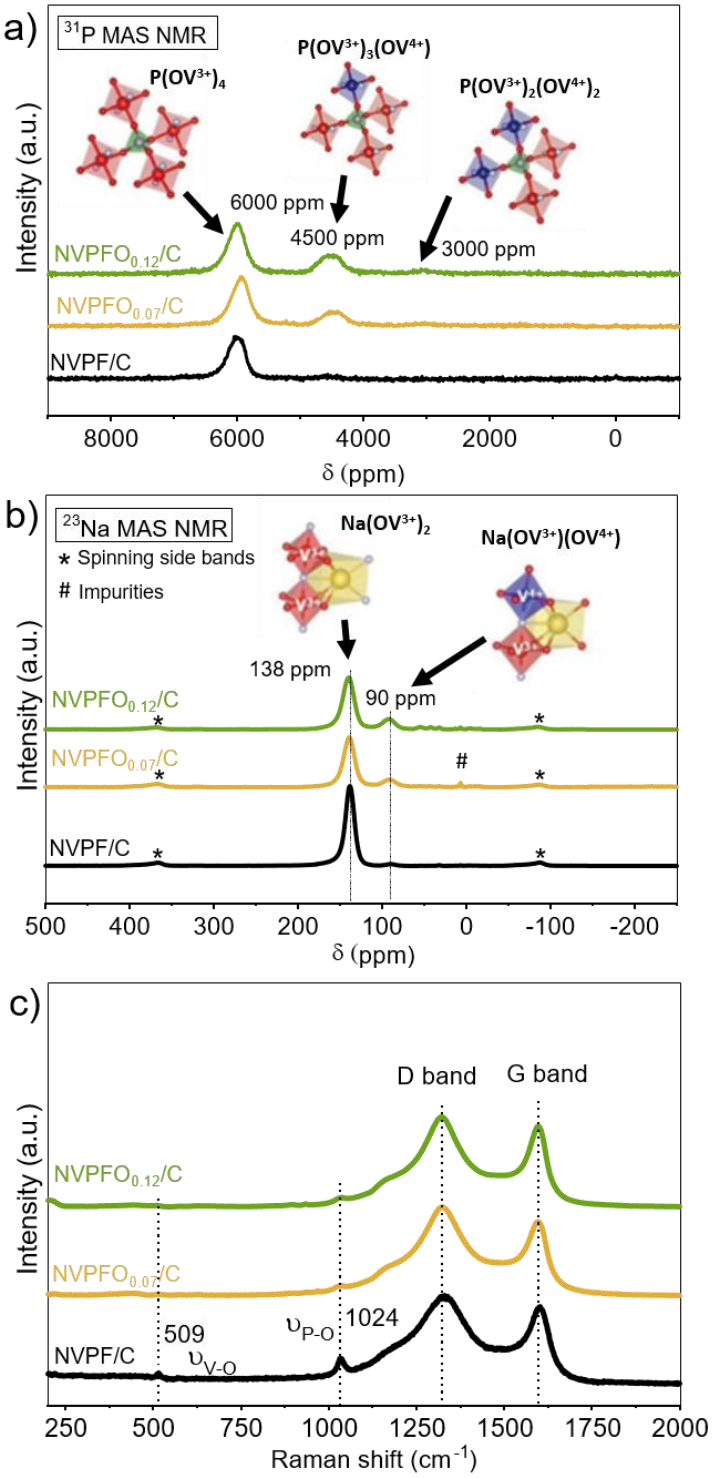

Figure 2: a) ^{31}P MAS NMR spectra of $Na_3V_2(PO_4)_2F_{3-y}O_y$/C phases (y = 0, 0.07 and 0.12) recorded at B_0 = 2.35 T with a 30 kHz MAS spinning frequency. PO_4 groups are represented as green tetrahedra, V^{3+} and V^{4+} octahedral units in red and blue, respectively. b) ^{23}Na MAS NMR spectra of $Na_3V_2(PO_4)_2F_{3-y}O_y$/C phases recorded at B_0 = 11.7 T with a 30 kHz MAS spinning frequency. c) Raman spectra of $Na_3V_2(PO_4)_2F_{3-y}O_y$/C phases

The ^{23}Na NMR spectra displayed in **figure 2b** confirm the observations made previously. The NVPF/C spectrum presents a main signal at 138 ppm attributed to a Na nucleus in close interaction with two V^{3+} ions.[41] For the $NVPFO_{0.07}$/C and $NVPFO_{0.12}$/C spectra, an additional signal at 90 ppm confirms the presence of Na close to a vanadium bi-octahedral unit with mixed V^{3+}/V^{4+} oxidation states.[43] Due to the small amount of V^{4+} in these two phases, the probability of having bi-octahedral units with two V^{4+} is statistically limited, explaining the very low intensity of the third signal at ~60 ppm characteristic of Na nucleus surrounded by two V^{4+} ions.

As complementary to NMR, results of Raman spectroscopy are presented in **figure 2c**. First, the broad signals at 1320 cm^{-1} and 1590 cm^{-1}, corresponding to D and G bands of carbon respectively, confirm the presence of a carbon coating for the three $NVPFO_y$/C phases.[44] In addition, the spectrum of NVPF/C displays two peaks at 509 cm^{-1} and 1024 cm^{-1} that are characteristic of vibrations of V-O bonds and phosphate groups respectively.[33] These two signals are barely detected for $NVPFO_{0.07}$/C and $NVPFO_{0.12}$/C, which might be explained by a more covering carbon coating than for NVPF/C and/or by the mixed V^{4+}/V^{3+} valence state leading to a distribution of vanadium local environments and thus to a peak broadening.[33]

Influence of O^{2-} for F^- substitution on the thermal stability at different states of charge of the battery.

The three studied electrode materials have been electrochemically desodiated (partially or fully) to obtain $Na_2V_2(PO_4)F_{3-y}O_y$ and $Na_1V_2(PO_4)F_{3-y}O_y$ compositions, respectively. Moreover, for each material a full cycle (charge and discharge) was performed (recovered material labelled as "discharged $NVPFO_y$"). The corresponding voltage-composition electrochemical data (recorded under galvanostatic mode) are given in **figures S3-S4.** The compositions of the recovered electrode materials were confirmed by PXRD (**figures S5-S6**).

Figures 3a-b show the ^{31}P and ^{23}Na NMR spectra of pristine $Na_3V_2(PO_4)_2F_3$/C, $Na_2V_2(PO_4)_2F_3$/C (Na2-charged material), $Na_1V_2(PO_4)_2F_3$/C (Na1-charged material) and $Na_3V_2(PO_4)_2F_3$/C (discharged NVPF/C). For both ^{31}P and ^{23}Na NMR measurements, the spectra of pristine and discharged materials are very similar, indicating that the $Na_3V_2(PO_4)_2F_3$/C composition is recovered after the first reversible cycle. For the Na2-charged material, the ^{31}P NMR spectra present a single peak at 3780 ppm indicating a V^{3+}/V^{4+} local charge ordering which confirms the $Na_2V^{3+}V^{4+}(PO_4)_2F_3$/C composition.[45] For ^{23}Na MAS NMR, a main signal is observed at 89 ppm assigned to Na surrounded by one V^{3+} and one V^{4+}. It is important to note that the mixed valence V^{3+}/V^{4+} results from a vanadium oxidation induced by Na^+ extraction and not from O^{2-} for F^- substitution. In that case, no specific electronic structure is expected for V^{4+} as not involved in vanadyl bonds. The Na1-charged material exhibits also single peaks located at 2500 ppm for ^{31}P and a main one at 40 ppm for ^{23}Na. Those signals are attributed to nuclei surrounded only by V^{4+} ions, confirming the full de-intercalation of the second sodium.[45]

Figures 3c-d exhibit ^{31}P and ^{23}Na NMR spectra of the pristine $Na_3V_2(PO_4)_2F_{2.88}O_{0.12}$/C, $Na_2V_2(PO_4)_2F_{2.88}O_{0.12}$/C (Na2-charged material), $Na_1V_2(PO_4)_2F_{2.88}O_{0.12}$/C (Na1-charged material) and $Na_3V_2(PO_4)_2F_{2.88}O_{0.12}$/C recovered after one cycle (discharged material). Similar observations than for NVPF/C can be made: pristine and end of discharge materials display the same signals at 6000 and 4500 ppm on ^{31}P NMR spectra and at 91 and 57 ppm on ^{23}Na NMR ones, attributed, as mentioned

previously, to $P(OV^{3+})_4$, $P(OV^{3+})_3P(OV^{4+})_1$, $Na(OV^{3+})_2$ and $Na(OV^{3+})(OV^{4+})$ local environments, respectively. Despite the high signal/noise ratio of the ^{31}P NMR spectra, one can observe broad single signals for the Na2-charged (3720 ppm) and Na1-charged (2700 ppm) materials assigned respectively to P surrounded by two V^{3+} and two V^{4+} ions and P surrounded by 4 V^{4+} ions. ^{23}Na MAS NMR also exhibits main signals at 91 ppm for Na-2 and at 57 ppm for Na-1 assigned to Na surrounded by one V^{3+} and one V^{4+} ions and Na surrounded by two V^{4+} ions respectively. The line broadening observed for ^{31}P and ^{23}Na may come from the coexistence of V^{4+} ions involved in vanadyl bonds and V^{4+} ions resulting from Na^+ deintercalation that have different electronic structures. Due to the low amount of V^{5+} ions expected for the Na-1 composition, new environments are not clearly seen, here.

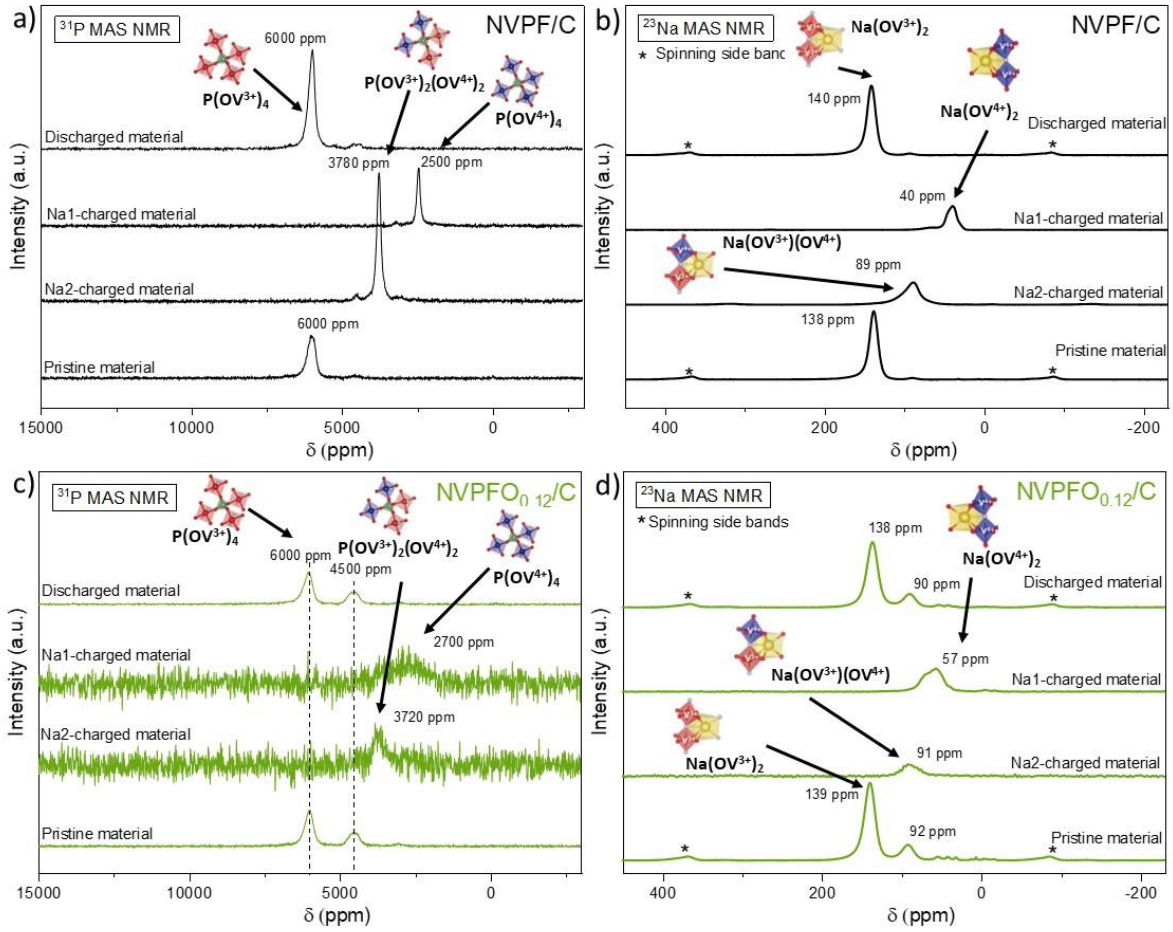

Figure 3: a-b) ^{31}P MAS NMR spectra and ^{23}Na MAS NMR spectra of NVPF/C at different states of charge or discharge: pristine, de-intercalated until Na2 (3.98 V *vs* Na^+/Na), de-intercalated until Na1 (4.3 V *vs* Na^+/Na), and de-intercalated until Na1 and re-intercalated (2.5 V *vs* Na^+/Na). c-d) ^{31}P and ^{23}Na MAS NMR spectra of $NVPFO_{0.12}/C$ at different states of charge or discharge: pristine, de-intercalated until Na2 (3.98 V *vs* Na^+/Na), de-intercalated until Na1 (4.3 V *vs* Na^+/Na), and de-intercalated until Na1 and re-intercalated (2.5V *vs* Na^+/Na).

The impact of a low amount of oxygen for fluorine substitution on the thermal stability of $Na_3V^{3+}_{2-y}V^{4+}_y(PO_4)_2F_{3-y}O_y/C$ was investigated by DSC analyses of materials recovered at various states of charge and discharge and in contact with the electrolyte. The results are displayed in **figure 4** whereas **Table 2** summarizes the experimental data and shows the total enthalpy generated due to thermal reactions. DSC curves are characterized, for the pristine carbon-coated materials, by rather similar

profiles although pristine $NVPFO_{0.07}$/C and $NVPFO_{0.12}$/C start to degrade at slightly lower temperature than NVPF/C (~255°C for $NVPFO_{0.07}$/C and $NVPFO_{0.12}$/C versus ~265°C for NVPF/C) and through a slightly more exothermic reaction (**Table 2**). Nevertheless, it is worth mentioning that for pristine phases the impact of a partial anionic substitution appears as very limited. Compared to the literature, the experimental specific heats generated (**Table 2**) are of the same order of magnitude to that measured by Aurbach *et al.* for some usual positive electrode materials used for Li-ion batteries (between 230 and 460 $J.g^{-1}$).[46]

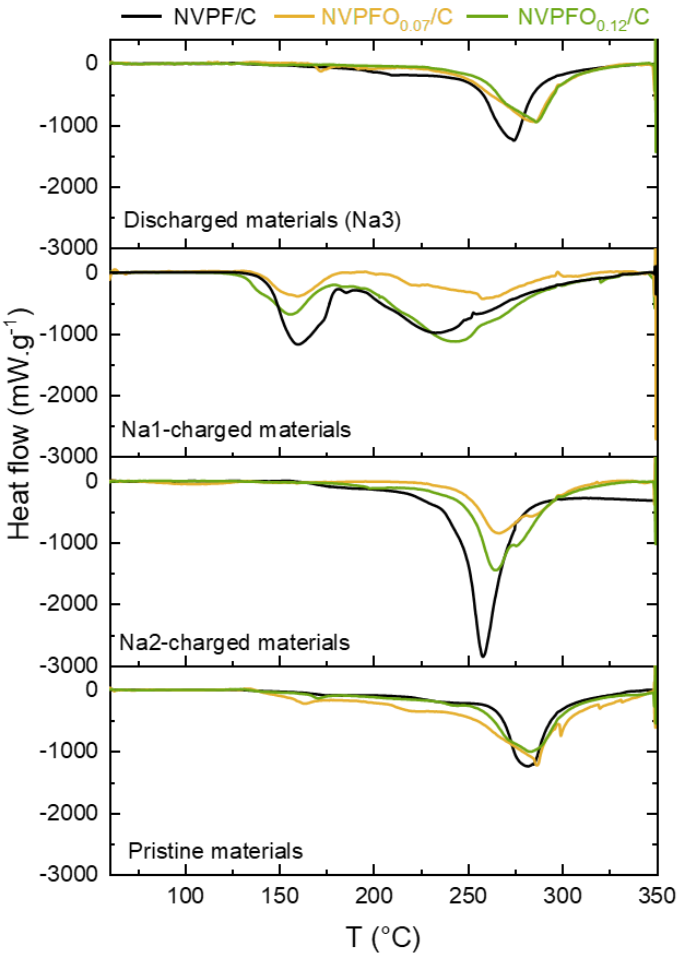

Figure 4: DSC curves of $Na_3V_2(PO_4)_2F_3$/C (black), $Na_3V_2(PO_4)_2F_{2.93}O_{0.07}$/C (yellow) and $Na_3V_2(PO_4)_2F_{2.88}O_{0.12}$/C (green) at different states of charge or discharge (from bottom to top: pristine materials, Na2-charged materials, Na1-charged materials and discharged materials (after one charge-discharge cycle)).

On the other hand, the oxygen for fluorine substitution has a beneficial effect on the thermal stability of Na2-charged $NVPFO_{0.07}$/C and Na2-charged $NVPFO_{0.12}$/C versus that of Na2-charged NVPF/C, with higher onset and peak decomposition temperatures and less pronounced exothermic effects. Furthermore, different degradation mechanisms would occur depending on the oxygen content in the $Na_3V_2(PO_4)_2F_{3-y}O_y$ ($0 \leq y \leq 2$) phases: a single peak is observed for NVPF/C whereas two broader and less intense overlapping exothermic peaks are observed for the partially substituted phases.

For all the fully Na1-charged carbon-coated materials, two distinct peaks are observed, and the degradation process starts at a much lower onset temperature: at ~145°C for NVPF/C and at even slightly lower temperature for $NVPFO_{0.07}$/C and $NVPFO_{0.12}$/C (140°C and 132°C, respectively). Samigullin *et al.* reported a much higher onset degradation temperature of 218.6°C for fully Na1-charged NVPF/C,

but these experiments are hardly comparable with ours as they were made on dry electrodes (without electrolyte).[28] The significantly lower enthalpy generated by the reaction demonstrates the safety benefits of partial oxygen for fluorine substitution in Na1-charged $NVPFO_y$-type phases. Finally, after one cycle (*i.e.* a charge and then a discharge), recovered materials show thermal degradation signatures similar to those observed for pristine materials, but with slightly lower degradation temperatures.

Table 2: Values of the first exothermic peak and onset temperatures, as well as the total heat generated as calculated from data depicted in **figure 4**

State of charge or discharge	Sample	Onset temperature (°C)	Peak temperature (°C)	Enthalpy ($J.g^{-1}$)
Pristine materials with 1M $NaPF_6$ in EC/DMC	NVPF/C	265	282	159
	$NVPFO_{0.07}$/C	252	287	180
	$NVPFO_{0.12}$/C	258	284	170
Na2-charged materials with 1M $NaPF_6$ in EC/DMC (cut-off potential: 3.98 V)	NVPF/C	247	259	329
	$NVPFO_{0.07}$/C	248	265 / 284	193
	$NVPFO_{0.12}$/C	250	264 / 277	270
Na1-charged materials with 1M $NaPF_6$ in EC/DMC (cut-off potential: 4.3 V)	NVPF/C	149	160 / 231	340
	$NVPFO_{0.07}$/C	140	159 / 259	177
	$NVPFO_{0.12}$/C	132	156 / 243	248
One cycle materials with 1M $NaPF_6$ in EC/DMC (cut-off potential: 2.5 V)	NVPF/C	255	275	155
	$NVPFO_{0.07}$/C	250	284	182
	$NVPFO_{0.12}$/C	256	286	185

Variations in the degradation mechanisms for NVPF/C

Pristine and Discharged NVPF/C: After DSC analyses, the XRD patterns of pristine and discharged NVPF/C materials show, as main reflexions, those of $Na_3V_2(PO_4)_2F_3$, but also as minor ones those of the electrolyte salt $NaPF_6$ and those of Na_3VF_6 (**Figure 5a** and **Table S1**). This later extra phase, present in very small amount, could be obtained as a by-product due to a reaction between NVPF and the electrolyte. This observation is in rather good agreement with the recent work of Mariyappan *et al.*, which demonstrates that vanadium dissolution in Na^+ de-intercalated NVPF is favoured in $NaPF_6$ based electrolyte containing controlled traces of H_2O and at moderated temperature.[47] The cells parameters of both pristine and discharged NVPF/C materials remain unchanged after DSC suggesting that the main phase is rather thermally stable and, most probably, only the surface reacts with the electrolyte/binder to form by-products. ^{31}P NMR and ^{23}Na NMR spectra confirm that both phosphorus and sodium environments within the NVPF-type phase barely evolved: a single ^{31}P signal is observed at 6000 ppm, and the ^{23}Na signal evolves from 138 ppm for the pristine material to 127 ppm for the discharged one (**figures 5b and 5c**). It should be noted that two groups of additional signals were detected around 50 and -10 ppm on ^{23}Na NMR spectra for pristine and discharged NVPF/C. They can

be attributed to Na_3VF_6 (50 ppm) and $NaPF_6$ or other diamagnetic degradation product (-10 ppm), in good agreement with PXRD.

Na2-charged NVPF/C: For the Na2-charged material recovered after the DSC experiment, all the diffraction peaks can be indexed within the *Amam* space group (before described in *Pmmm* (**Figure S5** and **Table S1**)). Quite surprisingly, the refined cell parameters correspond to those of the pristine $Na_3V_2(PO_4)_2F_3$ composition (**Figure 5a**) and no extra crystalline phases were detected this time. This implies that $NaPF_6$ reacts during the DSC experiment and contributes to regenerate the de-intercalated $Na_2V_2(PO_4)_2F_3$ electrode material to form $Na_3V_2(PO_4)_2F_3$. Moreover, the ^{31}P NMR spectrum of Na2-charged recovered after the DSC experiment (**Figure 5b**) displays a main signal at 6000 ppm (compared to 3780 ppm before DSC (**Figure3a**)) which validates the hypothesis of the formation of $Na_3V_2(PO_4)_2F_3$ during the thermal degradation. Similarly, the ^{23}Na NMR spectrum (**Figure 5c**), which displays a unique signal at 138 ppm, characteristic of $Na(OV^{3+})_2$ environments, undoubtedly confirm that $Na_3V_2(PO_4)_2F_3$ is recovered. Noteworthy, an additional ^{31}P signal is observed at 3000 ppm in addition to an increasing nonlinear background for the PXRD pattern, both suggesting the presence of an additional amorphous phase.

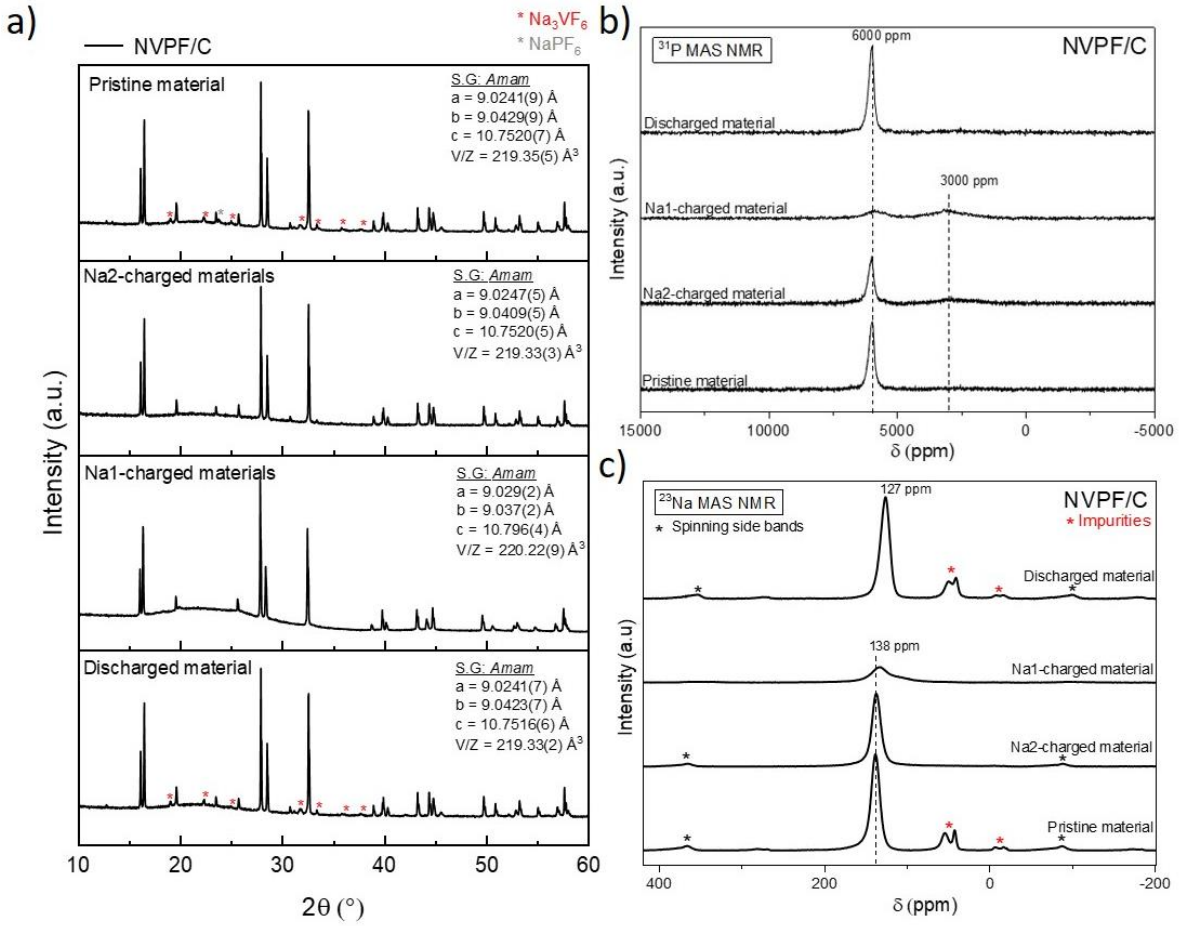

Figure 5: a) X-ray diffraction patterns of NVPF/C recovered at different states of charge or discharge and after DSC experiments, and the corresponding lattice and cell volume parameters determined by their Le Bail refinements. b) Corresponding ^{31}P MAS NMR spectra recorded at B_0 = 2.35 T and c) corresponding ^{23}Na MAS NMR spectra recorded at B_0 = 11.7 T with a MAS rate of 30 kHz.

***Na1-charged NVPF/C**:* From the DSC experiment, the lattice parameters of Na1-charged NVPF/C phase strongly evolved (a = 8.766(4) Å; b = 8.802(4) Å and c = 11.00(2) Å before DSC *vs* a = 9.029(2) Å; b = 9.037(2) Å and c = 10.796(4) Å after DSC) and become again rather close to those of $Na_3V_2(PO_4)_2F_3$ (**Table S1**). In addition, the presence of an amorphous phase, suggested by the PXRD pattern (**Figure 5a**), was confirmed on images recorded by TEM: it is localized at the surface of the particles forming an inhomogeneous coating of several tens of nanometers (**Figure 6**). Although the NMR signals are broader, the signals at 6000 ppm on the ^{31}P spectrum (**Figure 5b**) and at 138 ppm on the ^{23}Na one (**Figure 5c**) confirm also the formation of a $Na_3V_2(PO_4)_2F_3$-like phase after DSC, as observed by PXRD. The additional broad contribution around 3000 ppm observed on the ^{31}P NMR spectrum is most probably associated with the amorphous phase detected by X-ray diffraction and observed by TEM. The relative intensity of this signal increases from Na2-charged to Na1-charged NVPF/C, whereas the signal observed at 6000 ppm decreases and broadens. Indeed, from a rough estimation based on the Na-stoichiometry, the $Na_3V_2(PO_4)_2F_3$-type phase would correspond to 2/3 of the Na2-charged material after DSC, whereas to only 1/3 for the Na1-charged material.

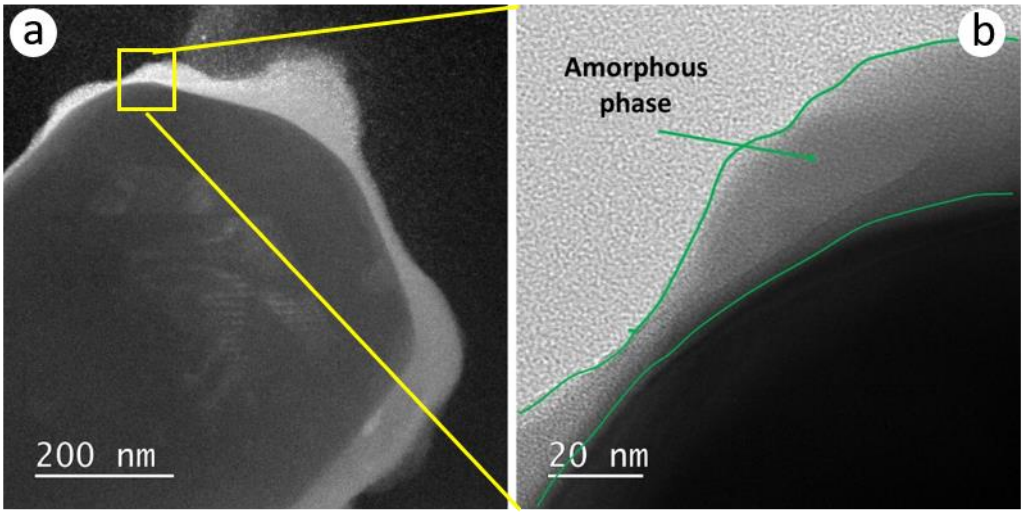

Figure 6: TEM images of Na1-charged NVPF/C recovered after DSC experiment. a) Dark field image showing the whole particle, b) Bright field higher magnification. The presence of an amorphous phase is clearly detected at particle surface. Unfortunately, this phase is not stable under the electron beam, which prevents from any further characterization.

The difference in cell parameters between pristine NVPF/C and the crystalline phase contained in Na1-charged NVPF/C recovered after DSC could be explained by an irreversible structural modification at high potential during the electrochemical floating performed to stabilize the Na1-charged phase. Indeed, this irreversible structural change was already reported by Nguyen *et al.* and characterized by *operando* XAS as a significant modification of the vanadium local environment.[39] Besides, Yan *et al.* also reported $Na_3V_2(PO_4)_2F_3$ with higher c-lattice parameter (~ 10.78 Å) after being cycled at high potential to partially extract the third Na^+, which is in good agreement with our results.[11]

PXRD and NMR data suggest that the thermal degradation of the active material $Na_xV_2(PO_4)_2F_3$ (x = 2, 1) in presence of electrolyte, PVdF and carbon black, leads to the formation of crystalline $Na_3V_2(PO_4)_2F_3$ and of an additional amorphous phase. To deeper understand the reaction mechanism and evaluate

the role/importance of $NaPF_6$, temperature-controlled XRD date were recorded, *in situ*, on $Na_1V_2(PO_4)_2F_3$/C without any electrolyte (after washing the electrode with DMC to remove all the traces of $NaPF_6$ electrolyte salt). The results are gathered in **Figure 7**.

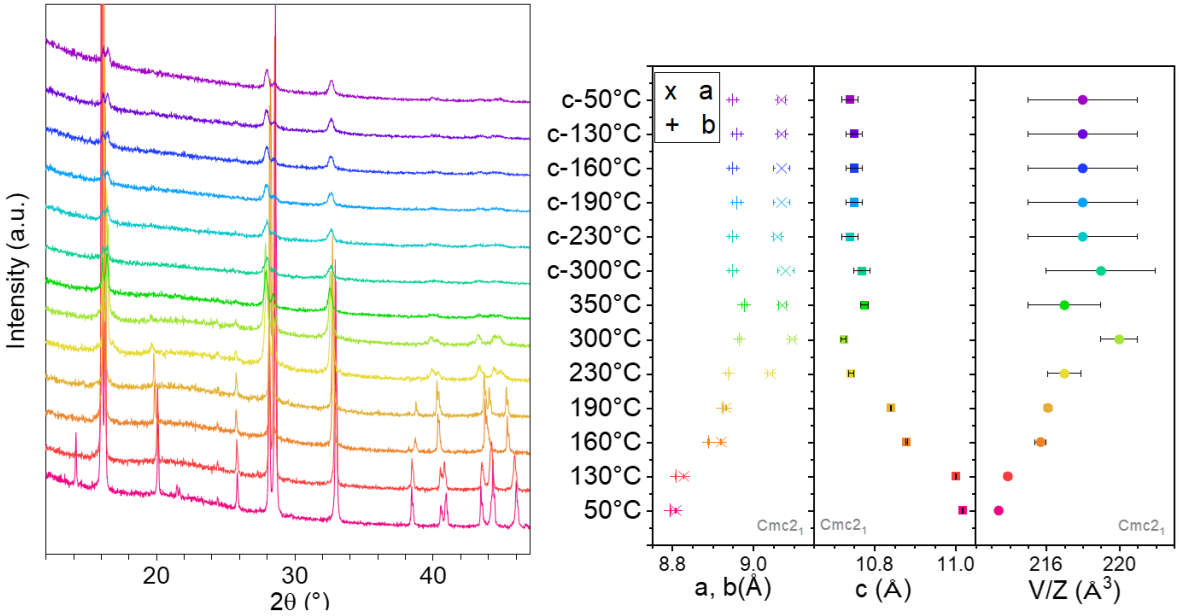

Figure 7: *In situ* X-ray diffraction patterns of $Na_1V_2(PO_4)_2F_3$/C at different temperatures and the corresponding lattice parameters determined by Le Bail refinements. c is for cooling.

The first PXRD pattern collected at 50°C displays a single phase whose structure can be described in the orthorhombic *Cmc2₁* space group with lattice parameters of a = 8.7958(7) Å, b = 8.8095(8) Å and c = 11.0177(6) Å, in perfect agreement with the $Na_1V_2(PO_4)_2F_3$ composition previously described [8]. Full pattern matching refinements of the recorded XRD data reveal a continuous evolution of the lattice parameters of the crystalline phase, when increasing the temperature up to 350°C, to finally reach lattice parameters very similar to those determined for the Na1-charged NVPF/C after the DSC experiment (here a = 9.00(1) Å, b = 9.05(1) Å and c = 10.78(1) Å, *vs* a = 9.029(2) Å; b = 9.037(2) Å and c = 10.796(4) Å after DSC). Moreover, a progressive line broadening is observed upon increasing the temperature. These results demonstrate that the formation of the crystalline $Na_3V_2(PO_4)_2F_3$ from $Na_1V_2(PO_4)_2F_3$ happens under thermal treatment, with or without the presence of $NaPF_6$ salt, next to an amorphous phase. Few is known about that latter phase except that it is amorphous, unstable under the electron beam, localized at the primary particles' surface and, finally, that it probably does not contain Na, as supported for instance by the ^{23}Na MAS NMR spectra. Attempts were done to use these post DSC phases as active material in new electrochemical cells versus metallic sodium, but they were poorly electrochemically active most probably due to the isolating amorphous layer covering the particles surface (**Figure S7**).

Degradation mechanisms for partially oxidized $NVPFO_y$: example of $NVPFO_{0.12}$/C

Similarly to NVPF/C, the PXRD patterns of pristine and discharged $NVPFO_{0.12}$ after the DSC experiment reveal the presence of $NaPF_6$ and Na_3VF_6 in addition to the dominant $NVPFO_y$-type phase (**Figure 8a**). However, quite surprisingly, the lattice parameters of the partially oxidized $NVPFO_{0.12}$ evolve after the thermal treatment and become very close to those of $Na_3V_2(PO_4)_2F_3$, suggesting a possible fluorination

(F^- for O^{2-} substitution) during the DSC experiment (**Table S1**). Likewise, the DSC thermal treatment of both half and fully charged $NVPFO_{0.12}$ leads to the formation of a crystalline phase whose PXRD pattern can be indexed in the *Amam* space group with cell parameters in perfect agreement with those of $Na_3V_2(PO_4)_2F_3$. It can also be seen on the XRD patterns that the DSC experiment leads to the formation of an amorphous phase in parallel to the crystalline one, as observed previously for NVPF/C. Another important point is that this time the lattice parameters of the fully discharged $NVPFO_{0.12}$ phase recovered after DSC are in perfect agreement with those of pristine NVPF (**Figure 8a** and **Table S1**). This output supports again the work of Nguyen *et al.* mentioning that a partial O^{2-} for F^- substitution prevents from irreversible structural modification during overcharge,[39] which is a great benefit for practical purposes. The analysis of the PXRD patterns of $NVPFO_{0.07}$/C presented in **figure S8** leads to the same outputs, confirming both that the conclusions made previously are valuable for electrode material possessing different oxygen contents in the $NVPFO_y$/C series.

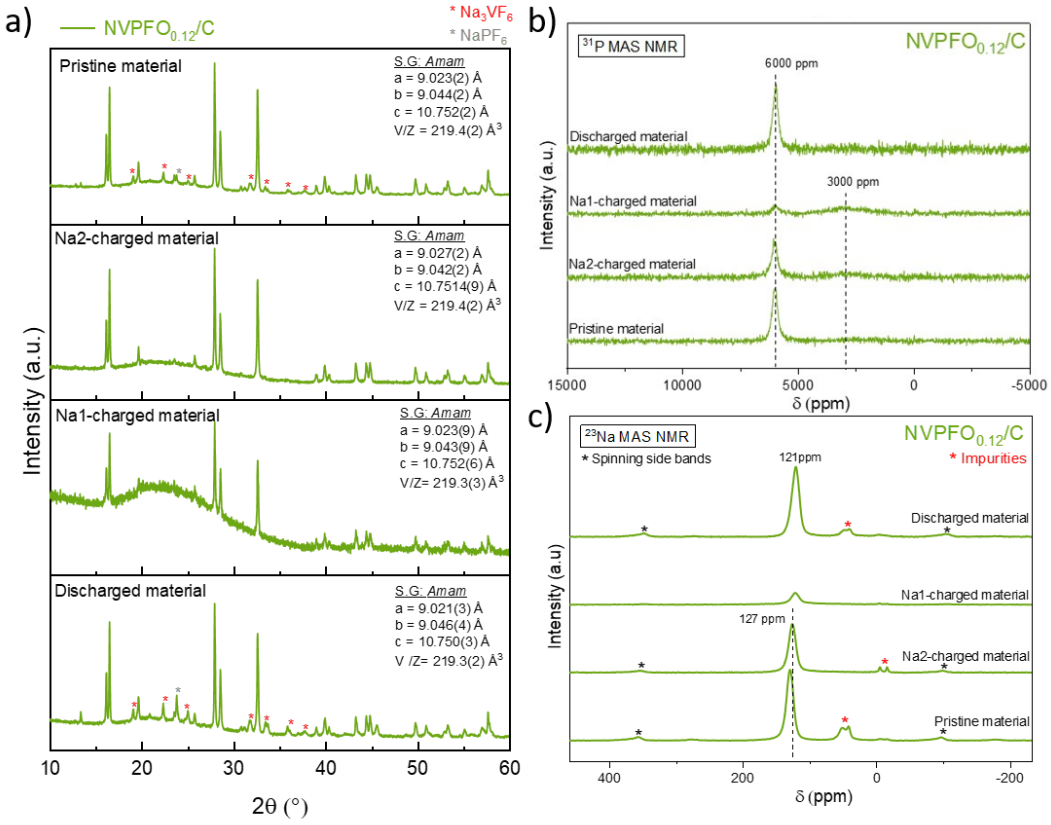

Figure 8: a) X-ray diffraction patterns of $NVPFO_{0.12}$/C at different states of charge or discharge, after DSC experiments, and the corresponding lattice parameters and unit cell volumes determined by Le Bail refinements. b) Corresponding ^{31}P MAS NMR spectra recorded at B_0 = 2.35 T and c) corresponding ^{23}Na MAS NMR spectra recorded at B_0 = 11.7 T with a NMR rate of 30 kHz.

ss-NMR investigations support the observations made previously for the partially oxidized electrode materials. For $NVPFO_{0.12}$, at each state of charge after DSC experiment, ^{31}P and ^{23}Na NMR spectra display a main signal respectively at ~6000 ppm attributed to $P(OV^{3+})_4$ and at ~130 ppm attributed to $Na(OV^{3+})_2$ confirming that crystalline $Na_3V_2(PO_4)_2F_3$ was recovered (**figures 8b-c**). The broad signal around 3000 ppm in the ^{31}P NMR spectrum and the resonances attributed to Na_3VF_6 and $NaPF_6$ impurities observed in the ^{23}Na NMR spectrum are observed too for Na2-charged $NVPFO_{0.12}$/C. Moreover, signals visible at ~4500 ppm for ^{31}P NMR and around 90 ppm for ^{23}Na NMR on pristine and discharged materials spectra, before DSC measurements (**Figures 2a-b**), and characteristic of $P(OV^{3+})_2(OV^{4+})_2$ and $Na(OV^{3+})(OV^{4+})$, are no longer observed after (**Figures 8b-c**). Due to the various

sources of fluorine ($NVPFO_{0.12}$, PVdF, $NaPF_6$), the chemical reaction that involves at the same time fluorination and vanadium reduction (for charge compensation during F^- for O^{2-} substitution) still needs to be determined. The binder, which can at the same time provide fluorine under decomposition and act as a reducing agent, drives most probably this fluorination reaction. This type of fluorination via a PTFE polymer was recently suggested by Sun *et al.* during the NVPF synthesis.[20]

Conclusion

A series of carbon-coated $Na_3V_2(PO_4)_2F_{3-y}O_y$ (y = 0, 0.07 and 0.12) materials were synthesized to investigate the impact of a low oxygen for fluorine substitution on the thermal stability of $NVPFO_y/C$ at different states of charge or discharge, and to understand the thermal degradation mechanisms in contact with electrolyte. Globally, the O^{2-} for F^- substitution has a very limited effect on the thermal stability of fully discharged materials, whereas it has a beneficial impact for charged ones. Indeed, the thermal degradation occurs at slightly higher temperature with less intense exothermic reaction for partially and fully charged electrode materials. Moreover, whatever the state of charge and the oxygen content in $Na_xV_2(PO_4)_2F_{3-y}O_y$ ($1 \leq x \leq 3$ and y = 0, 0.07 and 0.12), the thermal degradation leads, quite surprisingly, to the formation of crystalline $Na_3V_2(PO_4)_2F_3$ in addition to an amorphous phase. This reaction is similar with or without presence of electrolyte salt. The fluorination of the partially oxygen for fluorine substituted material was clearly demonstrated by PXRD and NMR on post DSC materials. Further investigations are currently done to understand more in detail the role of PVDF binder in the fluorination process and the vanadium reduction upon Na^+ re-intercalation.

Supporting Information

Pattern matching refinements, SEM images of the pristine materials, galvanostatic charge/discharge and XRD patterns of the materials recovered at different states of charge, Table with refined lattice parameters after DSC experiments.

Notes

The authors declare no competing financial interest.

Acknowledgement

The authors thank the European Union's Horizon 2020 research and innovation program under grant agreement No 875629 (NAIMA project), the French National Research Agency (STORE-EX Labex Project ANR-10-LABX-76-01 and the Project Nano-INSPIRE ANR-21-CE50-0006) and the financial support provided by Région Nouvelle Aquitaine. The authors thank Cathy DENAGE, Eric LEBRAUD and Jérôme KALISKY (ICMCB) for their technical support and Grégory Gachot (LRCS), Mathieu Morcrette (LRCS) and François Rabuel (LRCS) for fruitful discussions.

References

(1) Mariyappan, S.; Wang, Q.; Tarascon, J. M. Will Sodium Layered Oxides Ever Be Competitive for Sodium Ion Battery Applications? *J. Electrochem. Soc.* **2018**, *165* (16), A3714–A3722. https://doi.org/10.1149/2.0201816jes.

(2) Desai, P.; Huang, J.; Foix, D.; Tarascon, J. Zero Volt Storage of Na-Ion Batteries : Performance Dependence on Cell Chemistry ! *J. Power Sources* **2022**, *551* (October), 232177. https://doi.org/10.1016/j.jpowsour.2022.232177.

(3) Tarascon, J. Na-Ion versus Li-Ion Batteries: Complementarity Rather than Competitiveness. *Joule* **2020**, *4* (8), 1616–1620. https://doi.org/10.1016/j.joule.2020.06.003.

(4) Ponrouch, A.; Dedryvère, R.; Monti, D.; Demet, A. E.; Ateba Mba, J. M.; Croguennec, L.; Masquelier, C.; Johansson, P.; Palacín, M. R. Towards High Energy Density Sodium Ion Batteries through Electrolyte Optimization. *Energy Environ. Sci.* **2013**, *6* (8), 2361. https://doi.org/10.1039/c3ee41379a.

(5) Le Meins, J.-M.; Crosnier-Lopez, M.-P.; Hemon-Ribaud, A.; Courbion, G. Phase Transitions in the Na3M2(PO4)2F3 Family (M=Al3+, V3+, Cr3+, Fe3+, Ga3+): Synthesis, Thermal, Structural, and Magnetic Studies. *J. Solid State Chem.* **1999**, *148* (2), 260–277. https://doi.org/10.1006/jssc.1999.8447.

(6) Bianchini, M.; Brisset, N.; Fauth, F.; Weill, F.; Elkaim, E.; Suard, E.; Masquelier, C.; Croguennec, L. Na3V2(PO4)2F3 Revisited: A High-Resolution Diffraction Study. *Chem. Mater.* **2014**, *26* (14), 4238–4247. https://doi.org/10.1021/cm501644g.

(7) Song, W.; Ji, X.; Wu, Z.; Yang, Y.; Zhou, Z.; Li, F.; Chen, Q.; Banks, C. E. Exploration of Ion Migration Mechanism and Diffusion Capability for Na3V2(PO4)2F3 Cathode Utilized in Rechargeable Sodium-Ion Batteries. *J. Power Sources* **2014**, *256*, 258–263. https://doi.org/10.1016/j.jpowsour.2014.01.025.

(8) Bianchini, M.; Fauth, F.; Brisset, N.; Weill, F.; Suard, E.; Masquelier, C.; Croguennec, L. Comprehensive Investigation of the Na3V2(PO4)2F3-NaV2(PO4)2F3 System by Operando High Resolution Synchrotron X-Ray Diffraction. *Chem. Mater.* **2015**, *27* (8), 3009–3020. https://doi.org/10.1021/acs.chemmater.5b00361.

(9) Park, Y.-U.; Seo, D.-H.; Kim, H.; Kim, J.; Lee, S.; Kim, B.; Kang, K. A Family of High-Performance Cathode Materials for Na-Ion Batteries, Na 3 (VO 1− x PO 4) 2 F 1+2 x (0 ≤ x ≤ 1): Combined First-Principles and Experimental Study. *Adv. Funct. Mater.* **2014**, *24* (29), 4603–4614. https://doi.org/10.1002/adfm.201400561.

(10) Matts, I. L.; Dacek, S.; Pietrzak, T. K.; Malik, R.; Ceder, G. Explaining Performance-Limiting Mechanisms in Fluorophosphate Na-Ion Battery Cathodes through Inactive Transition-Metal Mixing and First-Principles Mobility Calculations. *Chem. Mater.* **2015**, *27* (17), 6008–6015. https://doi.org/10.1021/acs.chemmater.5b02299.

(11) Yan, G.; Mariyappan, S.; Rousse, G.; Jacquet, Q.; Deschamps, M.; David, R.; Mirvaux, B.; Freeland, J. W.; Tarascon, J.-M. Higher Energy and Safer Sodium Ion Batteries via an Electrochemically Made Disordered Na3V2(PO4)2F3 Material. *Nat. Commun.* **2019**, *10* (1), 585. https://doi.org/10.1038/s41467-019-08359-y.

(12) Dugas, R.; Zhang, B.; Rozier, P.; Tarascon, J. M. Optimization of Na-Ion Battery Systems Based on Polyanionic or Layered Positive Electrodes and Carbon Anodes. *J. Electrochem. Soc.* **2016**, *163* (6), A867–A874. https://doi.org/10.1149/2.0051605jes.

(13) Yi, H.; Lin, L.; Ling, M.; Lv, Z.; Li, R.; Fu, Q.; Zhang, H.; Zheng, Q.; Li, X. Scalable and Economic

Synthesis of High-Performance Na 3 V 2 (PO 4) 2 F 3 by a Solvothermal–Ball-Milling Method. *ACS Energy Lett.* **2019**, *4* (7), 1565–1571. https://doi.org/10.1021/acsenergylett.9b00748.

(14) Li, L.; Xu, Y.; Sun, X.; Chang, R.; Zhang, Y.; Zhang, X.; Li, J. Fluorophosphates from Solid-State Synthesis and Electrochemical Ion Exchange : NaVPO 4 F or Na 3 V 2 (PO 4) 2 F 3 ? *Adv. Energy Mater.* **2018**, *8*, 1801064. https://doi.org/10.1002/aenm.201801064.

(15) Broux, T.; Fauth, F.; Hall, N.; Chatillon, Y.; Bianchini, M.; Bamine, T.; Leriche, J.-B. J.; Suard, E.; Carlier, D.; Reynier, Y.; et al. High Rate Performance for Carbon-Coated Na 3 V 2 (PO 4) 2 F 3 in Na-Ion Batteries. *Small Methods* **2019**, *3* (4), 1800215. https://doi.org/10.1002/smtd.201800215.

(16) Fang, R.; Olchowka, J.; Pablos, C.; Camacho, P. S.; Carlier, D.; Croguennec, L.; Cassaignon, S. Effect of the Particles Morphology on the Electrochemical Performance of Na 3 V 2 (PO 4) 2 F 3-y O Y. *Batter. Supercaps* **2022**, *5* (1), 1–10. https://doi.org/10.1002/batt.202100179.

(17) Shen, X.; Zhao, J.; Li, Y.; Sun, X.; Yang, C.; Liu, H.; Hu, Y.-S. Controlled Synthesis of Na 3 (VOPO 4) 2 F Cathodes with an Ultralong Cycling Performance. *ACS Appl. Energy Mater.* **2019**, *2* (10), 7474–7482. https://doi.org/10.1021/acsaem.9b01458.

(18) Song, J.; Park, S.; Kim, S.; Mathew, V.; Alfaruqi, M. H.; Jo, J.; Kim, J. Uniform Carbon Coated Na 3 V 2 (PO 4) 2 O 2 x F 3–2 x Nanoparticles for Sodium Ion Batteries as Cathode. *ACS Sustain. Chem. Eng.* **2019**, *7* (23), 18826–18834. https://doi.org/10.1021/acssuschemeng.9b03584.

(19) Yu, X.; Lu, T.; Li, X.; Qi, J.; Yuan, L.; Man, Z.; Zhuo, H. Ionic Liquid–Acrylic Acid Copolymer Derived Nitrogen–Boron Codoped Carbon-Covered Na 3 V 2 (PO 4) 2 F 3 as Cathode Material of High-Performance Sodium-Ion Batteries. *Langmuir* **2022**, *38* (25), 7815–7824. https://doi.org/10.1021/acs.langmuir.2c01028.

(20) Sun, C.; Zhang, L.-L.; Deng, Z.-R.; Yan, B.; Gao, L.; Yang, X.-L. PTFE-Derived Carbon-Coated Na3V2(PO4)2F3 Cathode Material for High-Performance Sodium Ion Battery. *Electrochim. Acta* **2022**, No. 47, 141187. https://doi.org/10.1016/j.electacta.2022.141187.

(21) Olchowka, J.; Fang, R.; Bianchini Nuernberg, R.; Pablos, C.; Carlier, D.; Cassaignon, S.; Croguennec, L. Particle Nanosizing and Coating with an Ionic Liquid: Two Routes to Improve the Transport Properties of Na 3 V 2 (PO 4) 2 FO 2. *Nanoscale* **2022**, *14* (24), 8663–8676. https://doi.org/10.1039/D2NR01080A.

(22) Mukherjee, A.; Sharabani, T.; Sharma, R.; Okashy, S.; Noked, M. Effect of Crystal Structure and Morphology on Na3V2(PO4)2F3 Performances for Na-Ion Batteries. *Batter. Supercaps* **2020**, *3* (6), 510–518. https://doi.org/10.1002/batt.201900202.

(23) Ponrouch, A.; Marchante, E.; Courty, M.; Tarascon, J. M.; Palacín, M. R. In Search of an Optimized Electrolyte for Na-Ion Batteries. *Energy Environ. Sci.* **2012**, *5* (9), 8572–8583. https://doi.org/10.1039/c2ee22258b.

(24) Hou, D.; Xu, Z.; Yang, Z.; Kuai, C.; Du, Z.; Sun, C.-J.; Ren, Y.; Liu, J.; Xiao, X.; Lin, F. Effect of the Grain Arrangements on the Thermal Stability of Polycrystalline Nickel-Rich Lithium-Based Battery Cathodes. *Nat. Commun.* **2022**, *13* (1), 3437. https://doi.org/10.1038/s41467-022-30935-y.

(25) Pender, J. P.; Jha, G.; Youn, D. H.; Ziegler, J. M.; Andoni, I.; Choi, E. J.; Heller, A.; Dunn, B. S.; Weiss, P. S.; Penner, R. M.; et al. Electrode Degradation in Lithium-Ion Batteries. *ACS Nano* **2020**, *14* (2), 1243–1295. https://doi.org/10.1021/acsnano.9b04365.

(26) Huang, Y.; Lin, Y.-C.; Jenkins, D. M.; Chernova, N. A.; Chung, Y.; Radhakrishnan, B.; Chu, I.-H.; Fang, J.; Wang, Q.; Omenya, F.; et al. Thermal Stability and Reactivity of Cathode Materials for

Li-Ion Batteries. *ACS Appl. Mater. Interfaces* **2016**, *8* (11), 7013–7021. https://doi.org/10.1021/acsami.5b12081.

(27) Barkholtz, H. M.; Preger, Y.; Ivanov, S.; Langendorf, J.; Torres-Castro, L.; Lamb, J.; Chalamala, B.; Ferreira, S. R. Multi-Scale Thermal Stability Study of Commercial Lithium-Ion Batteries as a Function of Cathode Chemistry and State-of-Charge. *J. Power Sources* **2019**, *435* (July), 226777. https://doi.org/10.1016/j.jpowsour.2019.226777.

(28) Samigullin, R. R.; Drozhzhin, O. A.; Antipov, E. V. Comparative Study of the Thermal Stability of Electrode Materials for Li-Ion and Na-Ion Batteries. *ACS Appl. Energy Mater.* **2022**, *5* (1), 14–19. https://doi.org/10.1021/acsaem.1c03151.

(29) Bordes, A.; Marlair, G.; Zantman, A.; Chesnaye, A.; Lore, P.-A. Le; Lecocq, A. Safety Evaluation of a Sodium-Ion Cell: Assessment of Vent Gas Emissions under Thermal Runaway. *ACS Energy Lett.* **2022**, *7* (10), 3386–3391. https://doi.org/10.1021/acsenergylett.2c01667.

(30) Serras, P.; Palomares, V.; Goñi, A.; Kubiak, P.; Rojo, T. Electrochemical Performance of Mixed Valence Na3V2O2x(PO4)2F3−2x/C as Cathode for Sodium-Ion Batteries. *J. Power Sources* **2013**, *241*, 56–60. https://doi.org/10.1016/j.jpowsour.2013.04.094.

(31) Qi, Y.; Mu, L.; Zhao, J.; Hu, Y.; Liu, H.; Dai, S. Superior Na-Storage Performance of Low-Temperature-Synthesized Na 3 (VO 1− x PO 4) 2 F 1+2 x (0≤ x ≤1) Nanoparticles for Na-Ion Batteries. *Angew. Chemie Int. Ed.* **2015**, *54* (34), 9911–9916. https://doi.org/10.1002/anie.201503188.

(32) Zhao, J.; Mu, L.; Qi, Y.; Hu, Y.-S.; Liu, H.; Dai, S. A Phase-Transfer Assisted Solvo-Thermal Strategy for Low-Temperature Synthesis of Na 3 (VO 1−x PO 4) 2 F 1+2x Cathodes for Sodium-Ion Batteries. *Chem. Commun.* **2015**, *51* (33), 7160–7163. https://doi.org/10.1039/C5CC01504A.

(33) Fang, R.; Olchowka, J.; Pablos, C.; Bianchini Nuernberg, R.; Croguennec, L.; Cassaignon, S. Impact of the F – for O 2– Substitution in Na 3 V 2 (PO 4) 2 F 3– y O y on Their Transport Properties and Electrochemical Performance. *ACS Appl. Energy Mater.* **2022**, *5* (1), 1065–1075. https://doi.org/10.1021/acsaem.1c03446.

(34) Olchowka, J.; Nguyen, L. H. B.; Broux, T.; Sanz Camacho, P.; Petit, E.; Fauth, F.; Carlier, D.; Masquelier, C.; Croguennec, L. Aluminum Substitution for Vanadium in the Na3V2(PO4)2F3 and Na3V2(PO4)2FO2 Type Materials. *Chem. Commun.* **2019**, *55* (78), 11719–11722. https://doi.org/10.1039/c9cc05137f.

(35) Sun, X.; Wang, Z.; Hu, Q.; Mei, X.; Zhao, Y.; Ndahimana, A.; Geng, T.; Cui, J. Oxygen-Tuned Na 3 V 2 (PO 4) 2 F 3–2 y O 2 y (0 ≤ y < 1) as High-Rate Cathode Materials for Rechargeable Sodium Batteries. *ACS Appl. Energy Mater.* **2022**, *2*. https://doi.org/10.1021/acsaem.2c03347.

(36) He, J.; Tao, T.; Yang, F.; Sun, Z. Manipulating the Phase Compositions of Na 3 (VO 1– x PO 4) 2 F 1+2 x (0 ≤ x ≤ 1) and Their Synergistic Effects with Reduced Graphene Oxide toward High-Rate Sodium-Ion Batteries. *ACS Appl. Mater. Interfaces* **2021**, *13* (50), 60099–60114. https://doi.org/10.1021/acsami.1c21271.

(37) Qi, Y.; Mu, L.; Zhao, J.; Hu, Y.-S.; Liu, H.; Dai, S. Superior Na-Storage Performance of Low-Temperature-Synthesized Na 3 (VO 1− x PO 4) 2 F 1+2 x (0≤ x ≤1) Nanoparticles for Na-Ion Batteries. *Angew. Chemie Int. Ed.* **2015**, *54* (34), 9911–9916. https://doi.org/10.1002/anie.201503188.

(38) Nguyen, L. H. B.; Iadecola, A.; Belin, S.; Olchowka, J.; Masquelier, C.; Carlier, D.; Croguennec, L. A Combined Operando Synchrotron X-Ray Absorption Spectroscopy and First-Principles

Density Functional Theory Study to Unravel the Vanadium Redox Paradox in the Na 3 V 2 (PO 4) 2 F 3 –Na 3 V 2 (PO 4) 2 FO 2 Compositions. *J. Phys. Chem. C* **2020**, *124* (43), 23511–23522. https://doi.org/10.1021/acs.jpcc.0c06967.

(39) Nguyen, L. H. B.; Broux, T.; Camacho, P. S.; Denux, D.; Bourgeois, L.; Belin, S.; Iadecola, A.; Fauth, F.; Carlier, D.; Olchowka, J.; et al. Stability in Water and Electrochemical Properties of the Na3V2(PO4)2F3 – Na3(VO)2(PO4)2F Solid Solution. *Energy Storage Mater.* **2019**, *20* (February), 324–334. https://doi.org/10.1016/j.ensm.2019.04.010.

(40) Olchowka, J.; Nguyen, L. H. B.; Petit, E.; Camacho, P. S.; Masquelier, C.; Carlier, D.; Croguennec, L. Ionothermal Synthesis of Polyanionic Electrode Material Na 3 V 2 (PO 4) 2 FO 2 through a Topotactic Reaction. *Inorg. Chem.* **2020**, *59* (23), 17282–17290. https://doi.org/10.1021/acs.inorgchem.0c02546.

(41) Nguyen, L. H. B.; Sanz Camacho, P.; Broux, T.; Olchowka, J.; Masquelier, C.; Croguennec, L.; Carlier, D. Density Functional Theory-Assisted 31 P and 23 Na Magic-Angle Spinning Nuclear Magnetic Resonance Study of the Na 3 V 2 (PO 4) 2 F 3 –Na 3 V 2 (PO 4) 2 FO 2 Solid Solution: Unraveling Its Local and Electronic Structures. *Chem. Mater.* **2019**, *31* (23), 9759–9768. https://doi.org/10.1021/acs.chemmater.9b03546.

(42) Broux, T.; Bamine, T.; Fauth, F.; Simonelli, L.; Olszewski, W.; Marini, C.; Ménétrier, M.; Carlier, D.; Masquelier, C.; Croguennec, L. Strong Impact of the Oxygen Content in Na3V2(PO4)2F3– y Oy (0 ≤ y ≤ 0.5) on Its Structural and Electrochemical Properties. *Chem. Mater.* **2016**, *28* (21), 7683–7692. https://doi.org/10.1021/acs.chemmater.6b02659.

(43) Serras, P.; Palomares, V.; Alonso, J.; Sharma, N.; López del Amo, J. M.; Kubiak, P.; Fdez-Gubieda, M. L.; Rojo, T. Electrochemical Na Extraction/Insertion of Na 3 V 2 O 2 x (PO 4) 2 F 3–2 X. *Chem. Mater.* **2013**, *25* (24), 4917–4925. https://doi.org/10.1021/cm403679b.

(44) Semykina, D. O.; Kirsanova, M. A.; Volfkovich, Y. M.; Sosenkin, V. E.; Kosova, N. V. Porosity, Microstructure and Electrochemistry of Na3V2(PO4)2F3/C Prepared by Mechanical Activation. *J. Solid State Chem.* **2021**, *297*, 122041. https://doi.org/10.1016/j.jssc.2021.122041.

(45) Nguyen, L. H. B.; Camacho, P. S.; Fondard, J.; Carlier, D.; Croguennec, L.; Palacin, M. R.; Ponrouch, A.; Courrèges, C.; Dedryvère, R.; Trad, K.; et al. First 18650-Format Na-Ion Cells Aging Investigation: A Degradation Mechanism Study. *J. Power Sources* **2022**, *529* (January), 231253. https://doi.org/10.1016/j.jpowsour.2022.231253.

(46) Martha, S. K.; Haik, O.; Zinigrad, E.; Exnar, I.; Drezen, T.; Miners, J. H.; Aurbach, D. On the Thermal Stability of Olivine Cathode Materials for Lithium-Ion Batteries. *J. Electrochem. Soc.* **2011**, *158* (10), A1115. https://doi.org/10.1149/1.3622849.

(47) Desai, P.; Forero-Saboya, J.; Meunier, V.; Rousse, G.; Deschamps, M.; Abakumov, A. M.; Tarascon, J.; Mariyappan, S. Mastering the Synergy between Na3V2(PO4)2F3 Electrode and Electrolyte: A Must for Na-Ion Cells. *Energy Storage Mater.* **2023**, *57* (January), 102–117. https://doi.org/10.1016/j.ensm.2023.02.004.

Table of Contents Graphic